Image-Based Radar Cross-Section Synthesis for a Cluster of Multiple Static Targets

Takuma Watanabe, *Member, IEEE*

***Abstract*—In this article, we propose a novel image-based method for radar cross-section (RCS) prediction of a cluster of multiple static targets by synthesizing replicas of an original radar image. In this approach, we first measure the near-field backscattering of a target and reconstruct a corresponding radar image. Then, modified copies of this image with rotation, translation, and spatial filtering, are generated according to the predefined desired arrangement, and they are coherently summed to create a single synthesized image in which all scattering contributions contained in the modified images are virtually included. Finally, the synthesized image is utilized to predict the far-field RCS of the multiple targets, based on the theory of image-based near-field-to-far-field transformation (NFFFT). By employing the proposed algorithm, we can avoid building multiple test targets, resulting in the reduction of the production costs of them. Moreover, we can easily test several different experimental layouts of the multiple targets without repeating a real measurement. Numerical simulations and experiments are provided to demonstrate the validity of the proposed image-based RCS synthesis.**

***Index Terms*—Radar cross-section (RCS), multiple targets, near-field-to-far-field transformation (NFFFT), synthetic aperture imaging**

I. Introduction

COST-effective radar cross-section (RCS) testing is important in developing radar hardware and signal processing algorithms. As is well-known, RCS is normally defined in the far-field distance which is proportional to the dimension of the target and inversely proportional to the operating wavelength. Therefore, direct measurement of the RCS of an electrically large target is usually difficult owing to the requirement of a large test range and the high costs for building the measurement facility.

To deal with the aforementioned problems, several near-field-to-far-field transformation (NFFFT) algorithms [1]–[13] have been developed to achieve the near-field RCS measurement without requiring a large test site. One major approach is the "image-based NFFFT" [6]–[12] where we generate a radar image of a target based on the synthetic aperture signal processing. By considering the reconstructed image as a distribution of point scatterers, one can predict the backscattered field at an arbitrary location including the far-field region in which the RCS is defined.

The majority of existing literature considers RCS prediction and measurement of a unit target. However, as presented in [14], [15], a scene to be measured is not necessarily constituted by a single object, and one may need to evaluate the RCS of a cluster of multiple targets. In this case, different problems arise; that is, costs for manufacturing multiple test objects and effort to try several experiments under different arrangements of the targets. In this article, we propose a novel approach for RCS synthesis to estimate the backscattering of a cluster of multiple static targets based on the image-based NFFFT to solve these problems.

The basic idea of the proposed algorithm is quite simple as follows: Fist, we measure the near-field backscattering of a real target and reconstruct a corresponding radar image. Then, modified replicas of this original image with rotation, translation, and spatial filtering are generated according to the predefined scenario, and they are coherently summed to create a single synthesized image in which all scattering contributions in the replicated images are included. This synthesized image virtually represents a scene of multiple targets. Finally, the synthesized image is utilized to predict the far-field RCS of the multiple targets, based on the theory of the image-based NFFFT [6]–[12]. The development of this RCS synthesizing algorithm and its experimental validation are the main novelty and contribution of this article.

A similar topic was treated in [14], [15], where an RCS pattern of a single metallic aircraft model simulated using a numerical electromagnetic solver was used to synthesize the RCS of a scene containing multiple targets with identical shape. In this previous research work, a complex-valued backscattering pattern of a single target was replicated with multiplication of an appropriate phase factor of the assumed arrangement, and the modified replicas are coherently summed to synthesize the RCS of the multiple targets. This algorithm was based on the idea of array factor in the field of antenna arrays. The objective was to avoid rigorous calculation of the RCS of multiple targets to reduce the computational burden. On the other hand, the novel approach proposed in this article is intended to be applied for experimental data. Moreover, by generating a radar image of a target, spatial filtering [2], [16], [18] can be applied to extract or reject a desired part of the target, which is a distinctive advantage of the radar imaging.

The remainder of this article is organized as follows. In Section II, we briefly review the image-based RCS determination. Section III describes the proposed image-based RCS synthesis accompanied by simple numerical examples. Based on the developed theory, Section IV discuss the experimental validation carried out in an anechoic chamber. In this measurement, metallic trihedral reflectors and aircraft models are used for the demonstration of the proposed algorithm. Finally, Section V concludes the research presented in this article.

Manuscript received xxxx xx, xxxx; revised xxxx xx, xxxx; accepted xxxx xx, xxxx. Date of publication xxxx xx, xxxx; date of current version xxxx xx, xxxx, The Associate Editor coordinating the review process was X. Xxxx. *(Corresponding author: Takuma Watanabe.)*

Takuma Watanabe is with Fujitsu System Integration Laboratories Ltd., Kawasaki 211-8588, Japan (e-mail: takuma.watanabe.jp@ieee.org).

Digital Object Identifier xxxxx/xxxxx

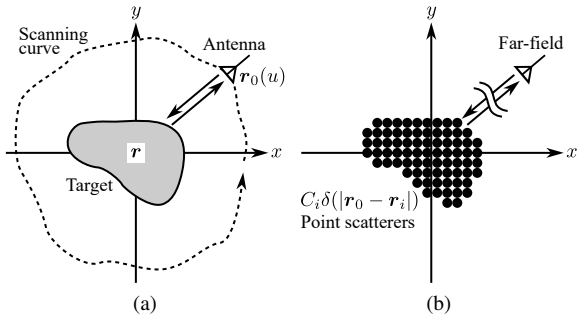

Fig. 1. Concept of the RCS determination with the image-based NFFFT. (a) Backscattering measurement with an arbitrary antenna-scanning curve. (b) Representation of a target with a cloud of point scatterers.

II. Image-Based RCS Determination

In this section, we briefly review the image-based RCS determination [6]–[12]. Fig. 1 illustrates a system model of near-field RCS measurement with an arbitrary antenna-scanning curve. As shown in Fig. 1(a), a target under test is placed on the origin of the 2-D (x, y)-plane, and an antenna moves along an arbitrary curve enclosing the target. The antenna transmits an electromagnetic wave and receives the scattered wave from the target during the scanning, where the main antenna beam is maintained toward the target throughout the measurement.

In the image-based NFFFT, we model a target as a cloud of point scatterers with unknown reflectivity as depicted in Fig. 1(b), where the mutual interaction between the scatterers is ignored. This modeling is the so-called Born or single-scattering approximation [17] which is commonly employed in radar signal processing. Based on this model, we reconstruct the unknown reflection coefficients from the measured near-field backscattering. Once the reflectivity distribution are known, the scattered field at an arbitrary spatial location, including the far-field region in which the RCS is defined, can be determined. In the following, we formulate the aforementioned approach.

A. Signal Model

As shown in Fig. 1, we consider the 2-D (x, y)-plane in which a target under test and an antenna are placed. The arbitrary antenna-scanning curve shown in Fig. 1(a) is denoted by a vector $\boldsymbol{r}_0(u)$ which is parametrized by a variable u, and an arbitrary spatial location is represented by a vector $\boldsymbol{r}$. These vectors are explicitly defined as follows:

$$\boldsymbol{r}_0(u) = x_0(u)\widehat{\boldsymbol{x}} + y_0(u)\widehat{\boldsymbol{y}} \tag{1a}$$

$$\boldsymbol{r} = x\widehat{\boldsymbol{x}} + y\widehat{\boldsymbol{y}}, \tag{1b}$$

where $\widehat{\boldsymbol{x}}$ and $\widehat{\boldsymbol{y}}$ are the unit vectors along x- and y-direction, respectively.

If the reflectivity at the point $\boldsymbol{r}$ is represented as a continuous function $C(\boldsymbol{r})$, the scattered wave received at an antenna location $\boldsymbol{r}_0(u)$ on the curve can be modeled as follows:

$$E^s(k, \boldsymbol{r}_0) = \frac{k^2}{\sqrt{4\pi}} \int_S P^2(k, \boldsymbol{r}_0, \boldsymbol{r}) C(\boldsymbol{r}) \frac{e^{-2jk|\boldsymbol{r}_0-\boldsymbol{r}|}}{|\boldsymbol{r}_0-\boldsymbol{r}|^2} d\boldsymbol{r}, \tag{2}$$

where S is the spatial domain of the integration; $k = \omega/c$ represents the wavenumber with the angular frequency ω and the wave propagation speed c; $P(k, \boldsymbol{r}, \boldsymbol{r}_0)$ is the antenna amplitude pattern in the direction from the antenna location $\boldsymbol{r}_0(u)$ toward the point $\boldsymbol{r}$. When the reflectivity $C(\boldsymbol{r})$ can be modeled as a sum of discrete point scatterers as illustrated in Fig. 1(b), the reflectivity function is expressed by

$$C(\boldsymbol{r}) = \sum_i C_i \delta(|\boldsymbol{r}-\boldsymbol{r}_i|) = \sum_i C_i \delta(x-x_i)\delta(y-y_i), \tag{3}$$

where C_i and $\boldsymbol{r}_i$ are the reflectivity and location of the ith point scatterer, respectively, and $\delta(\cdot)$ is the delta function. Substituting Eq. (3) into Eq. (2) yields the following expression:

$$E^s(k, \boldsymbol{r}_0) = \frac{k^2}{\sqrt{4\pi}} \sum_i P^2(k, \boldsymbol{r}_0, \boldsymbol{r}_i) C_i \frac{e^{-2jk|\boldsymbol{r}_0-\boldsymbol{r}_i|}}{|\boldsymbol{r}_0-\boldsymbol{r}_i|^2}. \tag{4}$$

Eq. (4) is the received signal model of a target composed of discrete point scatterers as shown in Fig. 1(b). This discrete scatterer model is used to numerically demonstrate the proposed approach in Section III.

B. Image Reconstruction

The next task is to reconstruct the reflectivity distribution $C(\boldsymbol{r})$ or C_i, which is what we call a "radar image," from the received signal $E^s(k, \boldsymbol{r}_0)$. The scatterer location $\boldsymbol{r}_i$ is assumed to be known as it is considered as a point on a Cartesian grid. As an example, we assume a single point scatterer at $\boldsymbol{r}_1 = (x_1, y_1)$. The ideal image for this scatterer is defined by Eq. (3) with $i = \{1\}$ as follows:

$$\psi(\boldsymbol{r}) = C_1 \delta(x-x_1)\delta(y-y_1). \tag{5}$$

The received signal corresponding to Eq. (5) is given by Eq. (4) with $i = \{1\}$ as follows:

$$E^s(k, \boldsymbol{r}_0) = \frac{k^2}{\sqrt{4\pi}} P^2(k, \boldsymbol{r}_0, \boldsymbol{r}_1) C_1 \frac{e^{-2jk|\boldsymbol{r}_0-\boldsymbol{r}_1|}}{|\boldsymbol{r}_0-\boldsymbol{r}_1|^2}. \tag{6}$$

The image reconstruction is generally accomplished by the following integral transformation of the received signal $E^s(k, \boldsymbol{r}_0)$ with a weighting function $F(k, \boldsymbol{r}_0, \boldsymbol{r})$:

$$\psi(\boldsymbol{r}) = \int_0^\infty \int_{\mathcal{D}} E^s(k, \boldsymbol{r}_0) F(k, \boldsymbol{r}_0, \boldsymbol{r})\, du\, dk, \tag{7}$$

where $\mathcal{D}$ is the domain of the integration with respect to u. The weighting function $F(k, \boldsymbol{r}_0, \boldsymbol{r})$ in Eq. (7) is referred to as the "focusing factor" and defined as

$$F(k, \boldsymbol{r}_0, \boldsymbol{r}) = g(k, \boldsymbol{r}_0, \boldsymbol{r}) \frac{|\boldsymbol{r}_0-\boldsymbol{r}|^2}{P^2(k, \boldsymbol{r}_0, \boldsymbol{r})} e^{2jk|\boldsymbol{r}_0-\boldsymbol{r}|}. \tag{8}$$

In Eq. (8), $g(k, \boldsymbol{r}_0, \boldsymbol{r})$ is called the "correction factor" [9]–[11] which is defined such that the integral transformation of Eq. (6) is reduced to the ideal image of a single point scatterer given in Eq. (5). The definition of the correction factor is [9]

$$g(k, \boldsymbol{r}_0, \boldsymbol{r}) = \frac{2}{\pi^{\frac{3}{2}} k} \left| \frac{d\alpha}{du} \right|, \tag{9}$$

where $\alpha(u)$ represents the local azimuth angle of the antenna viewed from the scatterer location $\boldsymbol{r}_1$, expressed as

$$\alpha(u) = \tan^{-1}[R_y(u)/R_x(u)], \tag{10}$$

with

$$R_x(u) = x_0(u) - x,\ R_y(u) = y_0(u) - y. \tag{11}$$

As discussed in [9]–[11], one can prove that the image reconstruction given in Eq. (7) reduces to the ideal image defined in Eq. (5) by incorporating the correction factor of Eq. (9) into the focusing factor of Eq. (8).

When the antenna-scanning curve shown in Fig. 1(a) is a simple circle of radius ρ_0 centered at the origin of the coordinate, the expression of the curve is given by

$$x_0(u) = \rho_0 \cos u,\ y_0(u) = \rho_0 \sin u. \tag{12}$$

In this case, the corresponding correction factor is explicitly derived as follows [9]:

$$g(k, \boldsymbol{r}_0, \boldsymbol{r}) = \frac{2\rho_0 \left| R_x \cos u + R_y \sin u \right|}{\pi^{3/2} k \left(R_x^2 + R_y^2 \right)}. \tag{13}$$

Note that an arbitrary scanning curve can be used by calculating the derivative in the correction factor of Eq. (9) via a numerical differentiation algorithm [10], [11].

C. RCS Determination

The final step of the image-based NFFFT is to compute the RCS from the reconstructed image. As depicted in Fig. 1(b), the reconstructed spatial image can be considered as a cloud of point scatterers, where now that the reflectivity of the ith scatterer C_i is known. Therefore, the scattered field at an arbitrary antenna location $\boldsymbol{r}_0$, including the far-field region in which the RCS is defined, can be recovered via Eq. (4).

The general definition of RCS is

$$\sigma\left(\boldsymbol{k}_r\right) = \lim_{r_0 \to \infty} 4\pi r_0^2 \left| \frac{E^s(k, \boldsymbol{r}_0)}{E^i(k, \boldsymbol{r}_0)} \right|^2, \tag{14}$$

where $r_0 = |\boldsymbol{r}_0|$, $\boldsymbol{k}_r = 2k\boldsymbol{r}_0/r_0$, and $E^i(k, \boldsymbol{r}_0)$ is the incident field. If we define the incident field as

$$E_0^i(k, \boldsymbol{r}_0) = \frac{e^{-jkr_0}}{r_0}, \tag{15}$$

the RCS can be computed as follows [9]–[11]:

$$\begin{aligned} \sigma\left(\boldsymbol{k}_r\right) &= k^4 \left| \int_{-\infty}^{\infty} \int_{-\infty}^{\infty} \psi(\boldsymbol{r}) \exp(j\boldsymbol{k}_r \cdot \boldsymbol{r})\, dx\, dy \right|^2 \\ &= k^4 \left| \mathcal{F}_{(x,y)}^{-1} \left[\psi(x, y) \right] \right|^2, \end{aligned} \tag{16}$$

where $\mathcal{F}_{(x,y)}^{-1}[\cdot]$ is the 2-D inverse Fourier transform with respect to the spatial variables (x, y). Therefore, once a radar image is obtained, the corresponding RCS is given by the 2-D inverse Fourier transform of that image.

III. Image-Based RCS Synthesis

In this section, we describe the proposed image-based RCS synthesis. A simple numerical simulation based on the discrete scatterer model of Eq. (4) is provided to demonstrate the proposed concept.

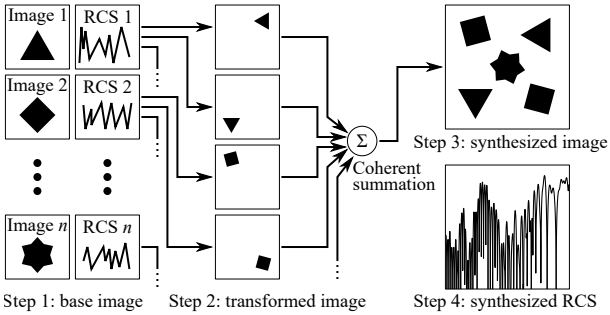

Fig. 2. Processing flow of the proposed image-based RCS synthesis.

A. Processing Flow

Fig. 2 represents the processing flow of the proposed image-based RCS synthesis. As illustrated in Fig. 2, an original radar image is repeatedly replicated with transformation (e.g., rotation, translation, and spatial filtering) to create multiple images, and they are coherently summed to generate a single image; then, we compute the corresponding RCS of the synthesized image according to Eq. (16). A step-by-step description of Fig. 2 is as follows:

1) As shown in Step 1 of Fig. 2, reconstruct an original radar image from the measured data based on Eq. (7). We refer to this image as a "base image." A single target or multiple targets can be contained in it.
2) The base image is duplicated and transformed to generate a new image. As discussed in the Sections III-D to III-E, possible image transformations are rotation, translation, and spatial filtering. This image is called a "transformed image." As illustrated in Step 2 of Fig. 2, multiple transformed images having different transformation parameters can be generated. Steps 1 and 2 are repeated for other desired targets, if any.
3) All the transformed images obtained through the above Steps 1 and 2 are coherently summed to create a single image, as shown in Step 3 of Fig. 2. This image is referred to as a "synthesized image" where all scattering contributions of the transformed images are virtually included. Note that the synthesized image can be used as a base image to generate another transformed image (i.e., a modified replica of the synthesized image).
4) Finally, we compute the corresponding RCS by Fourier-transforming the synthesized image according to Eq. (16) (Step 4 of Fig. 2). We refer to the obtained RCS as the "synthesized RCS."

The aforementioned algorithm is expressed as follows: We denote mth base image by $\psi_m(x, y), m \in \{1, 2, \ldots\}$, and we represent nth ($n \in \{1, 2, \ldots\}$) image transformation (i.e., rotation, translation, spatial filtering, and repetition and combination of them) operated on the mth image by $\mathcal{T}_{m,n}[\cdot]$. Then, the synthesized image $\psi_\Sigma(x, y)$ is written as

$$\psi_\Sigma(x, y) = \sum_m \sum_n \mathcal{T}_{m,n} \left[\psi_m(x, y) \right]. \tag{17}$$

By using Eq. (16) with $\psi(x, y) \to \psi_\Sigma(x, y)$, one can compute the synthesized RCS of the multiple targets.

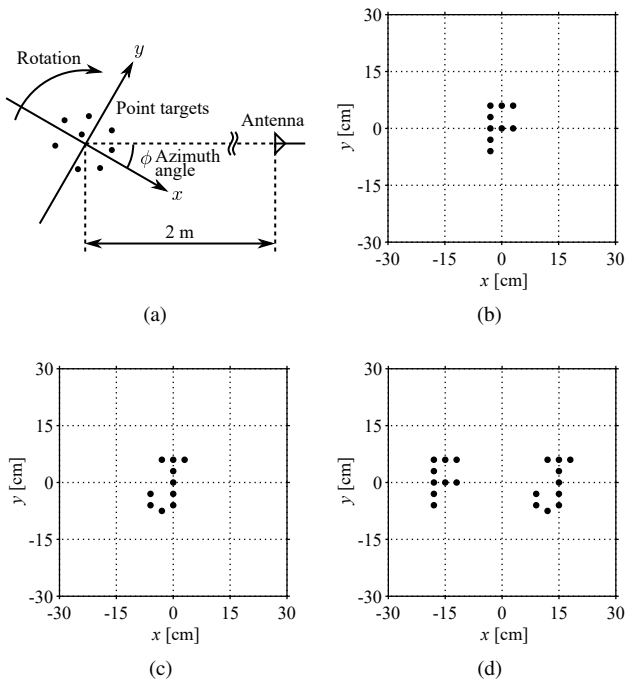

Fig. 3. Simulation setup and location of point scatterers. (a) Simulation setup. (b) F-shaped scatterer. (c) J-shaped scatterer. (d) FJ-shaped scatterer.

TABLE I
SIMULATION PARAMETERS

Center frequency	$10.2\,\mathrm{GHz}$
Bandwidth	$4\,\mathrm{GHz}$
Frequency sampling interval	$20\,\mathrm{MHz}$
Angular sampling interval	$0.4°$
Angular range	$[0°, 360°]$
Radius of trajectory	$2\,\mathrm{m}$

In the following discussion, we demonstrate the proposed approach by point-scatterer simulations.

B. Overview of the Simulation

The simulation is based on the discrete scatterer model defined in Eq. (4). Fig. 3 shows the simulation setup and the location of point scatterers, and Table I lists the simulation parameters. Note that these parameters were selected to ensure consistency with the experimental validation in Section IV.

As illustrated in Fig. 3(a), the point scatterers were distributed on a 2-D (x, y)-plane like in Fig. 1(b). The locations of the scatterers were designated in Figs. 3(b), (c), and (d), where the three types of arrangement, namely, "F"-, "J"-, and "FJ"-shaped objects were shown, respectively. The antenna was fixed at $2\,\mathrm{m}$ away from the origin of the coordinate, while the (x, y)-axes and the scatterers were rotated simultaneously to create a circular synthetic aperture. The antenna pattern was assumed to be isotropic. The center frequency and bandwidth were $10.2\,\mathrm{GHz}$ and $4\,\mathrm{GHz}$, respectively, and the angular sampling interval was $0.4°$. The received signals for each scatterer arrangement were generated based on Eq. (4), and the base images were reconstructed according to Eq. (7). The reflection coefficients C_i of these point scatterers were determined assuming the conductive spheres of equivalent radii $a_i = 1.5\,\mathrm{mm}$, as follows [9], [19]:

$$C_i = 3\sqrt{\pi} a_i^3 \tag{18}$$

Note that Eq. (18) is valid for a sphere having the radius sufficiently small compared to the wavelength (i.e., $ka_i < 0.4$).

C. Base Images

Figs. 4(a)–6(a) show the reconstructed base images for the arrangement presented in Figs. 3(b), (c), and (d), respectively, and Figs. 4(b)–6(b) show the corresponding RCS derived from the image shown in Figs. 4(a)–6(a), respectively. In Figs. 4(b)–6(b), the theoretical RCS is also plotted, of which the expression is defined as follows [9]:

$$\sigma = k^4 \left| \sum_i C_i \exp\left(jk_x x_i + jk_y y_i\right) \right|^2 \tag{19a}$$

$$k_x = 2k\cos\phi,\ \ k_y = 2k\sin\phi \tag{19b}$$

where ϕ represents the azimuth angle. Note that throughout this article, the RCS was computed at $10\,\mathrm{GHz}$. One can confirm from Figs. 4(b)–6(b) that the reconstructed RCS via the image-based NFFFT well agrees with those obtained from the theoretical expression of Eq. (19).

According to the algorithm described in Section III-A, several image transformations were applied to these base images, and synthesized images were generated by summing the multiple transformed images; then, the corresponding RCS was computed. To evaluate the effectiveness of the proposed RCS synthesis, we compared the RCS reconstructed from the synthesized image and those obtained from a "real image" which is generated from the received signal assuming that the point scatterers were deployed such that the arrangement was exactly same as those assumed in the synthesized scenario. We refer to the RCS of a real image as the "real RCS."

D. Image Rotation and Translation

In this section, we explain image rotation and translation algorithms which are suitable for our purpose. First, we describe the former operation. In digital image processing where an 2-D image is represented as a real-valued matrix, the image rotation is generally done via 2-D interpolation algorithms such as bi-nearest neighbor, bilinear, and bicubic interpolation.

Although such an approach can be used for a complex-valued radar image, the image rotation can be efficiently processed without interpolation based on the multiple 1-D Fourier transforms. As discussed in [21]–[23], the image rotation is represented as three shear operations, and these can be accomplished by the following six 1-D Fourier transforms [23]:

$$\psi_x(x, y) = \mathcal{F}_{(k_x)} \left[e^{-jk_x a y}\, \mathcal{F}^{-1}_{(x)} \left[\psi(x, y) \right] \right] \tag{20a}$$

$$\psi_{xy}(x, y) = \mathcal{F}_{(k_y)} \left[e^{-jk_y b x}\, \mathcal{F}^{-1}_{(y)} \left[\psi_x(x, y) \right] \right] \tag{20b}$$

$$\psi_\theta(x, y) = \mathcal{F}_{(k_x)} \left[e^{-jk_x a y}\, \mathcal{F}^{-1}_{(x)} \left[\psi_{xy}(x, y) \right] \right] \tag{20c}$$

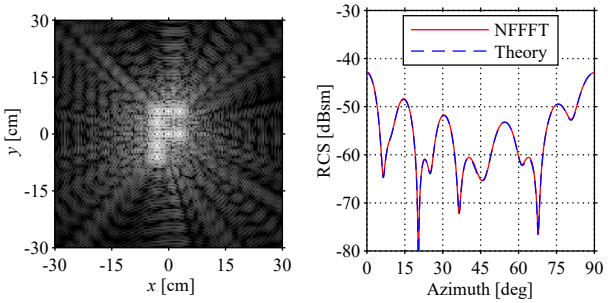

Fig. 4. Base image and RCS (F-shaped scatterer). (a) Spatial image. (b) RCS determined from (a).

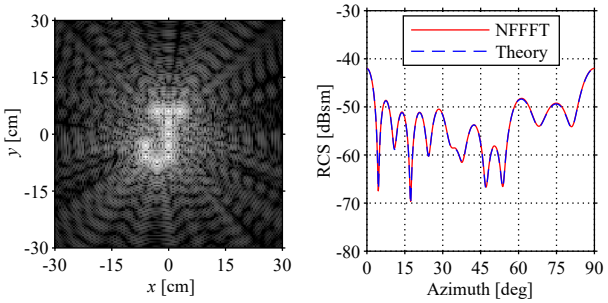

Fig. 5. Base image and RCS (J-shaped scatterer). (a) Spatial image. (b) RCS determined from (a).

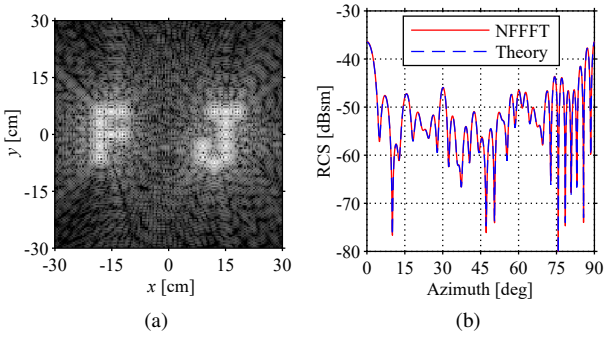

Fig. 6. Base image and RCS (FJ-shaped scatterer). (a) Spatial image. (b) RCS determined from (a).

where $\mathcal{F}_{(k_x)}[\cdot]$ is the 1-D Fourier transform with respect to the spatial frequency k_x, and $\mathcal{F}^{-1}_{(x)}[\cdot]$ is the 1-D inverse Fourier transform with respect to spatial variable x; similar definitions can be established for k_y and y; a and b are the amount of the shear in x- and y-direction, respectively. If the angle of rotation is θ, a and b are given by [21]–[23]

$$a = \tan(\theta/2), \;\; b = -\sin\theta. \tag{21}$$

In Eq. (20), $\psi_x(x,y)$, $\psi_{xy}(x,y)$, and $\psi_\theta(x,y)$ represent the image of the first shear in x-direction applied to the original image $\psi(x,y)$, the second shear in y-direction applied to the x-sheared image $\psi_x(x,y)$, and the final shear in x-direction applied to the (x,y)-sheared image $\psi_{xy}(x,y)$, respectively, where $\psi_\theta(x,y)$ is the desired θ-rotated image. As these Fourier

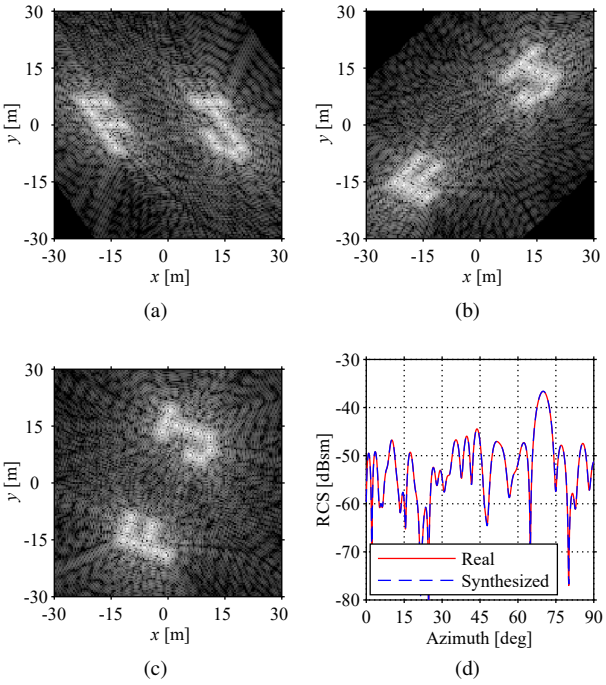

Fig. 7. Image rotated by three shears and the resultant RCS (FJ-shaped scatterer). The rotation angle was $\theta = 70°$. (a) First shear $\psi_x(x,y)$. (b) Second shear $\psi_{xy}(x,y)$. (c) Rotated spatial image $\psi_\theta(x,y)$. (d) RCS determined from (c).

transforms can be implemented by the fast Fourier transform (FFT), an efficient image rotation can be achieved [23].

It is worth mentioning that the aforementioned algorithm is valid for a rotation angle up to 90°. For an angle greater than 90°, an image must be rotated through an integer multiply of 90°, represented by $n\pi/2$ ($n \in \{1,2,3\}$), so that the remaining rotation angle is less than 90°; then, the rotation through $\theta - n\pi/2$ is processed. Alternatively, 90°-, 180°-, and 270°-rotated base images must be additionally reconstructed by replacing the azimuth angle $\phi_0 \to \phi_0 + n\pi/2$, followed by the shear-based rotation. Note that the aforementioned 2-D image rotation was extended to a 3-D case in [24].

Fig. 7 represents the process of image rotation and the RCS determined from the rotated image, where the FJ-shaped base image was used for this demonstration; the rotation angle was 70°. Figs. 7(a), (b), and (c) show the x-sheared image $\psi_x(x,y)$, (x,y)-sheared image $\psi_{xy}(x,y)$, and rotated image $\psi_\theta(x,y)$, respectively. One can confirm that the image rotation was correctly accomplished by Eq. (20) with Eq. (21). Fig. 7(d) shows the RCS reconstructed from the rotated image of Fig. 7(c), plotted with the real RCS (i.e., those reconstructed from the image of the FJ-shaped point scatterers placed on the 70°-rotated position) for reference. As these RCS patterns exactly agree with each other, the correctness of the image transformation is proved.

The latter operation, translation, can be readily accomplished based on the well-known shift property of the Fourier

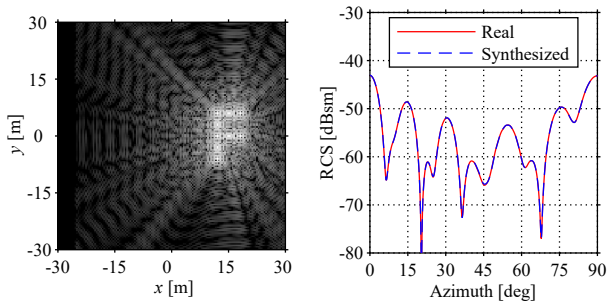

(a) (b)

Fig. 8. Translated image $\psi_{\parallel}(x, y)$ and RCS (F-shaped scatterer). (a) Spatial image. (b) RCS determined from (a).

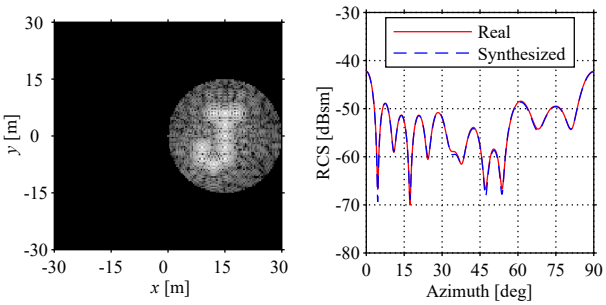

(a) (b)

Fig. 9. Band-pass filtered image and RCS (J-shaped scatterer created from FJ-shaped scatterer). (a) Spatial image. (b) RCS determined from (a).

transform, as follows:

$$\psi_{\parallel}(x, y) = \mathcal{F}_{(k_x,k_y)}\left[e^{-jk_x x' - jk_y y'}\,\mathcal{F}^{-1}_{(x,y)}\left[\psi(x, y)\right]\right] \quad (22)$$

where (x', y') represent the amount of translation with respect to x- and y-direction, respectively; $\mathcal{F}_{(x,y)}[\cdot]$ and $\mathcal{F}^{-1}_{(k_x,k_y)}[\cdot]$ are the 2-D forward and inverse spatial Fourier transform with respect to the variables (x, y) and (k_x, k_y), respectively.

Fig. 8(a) depicts the translated image of the F-shaped scatterer shown in Fig. 4(a), and Fig. 8(b) represents the corresponding RCS reconstructed from the translated image of Fig. 8(a). As the shape and orientation of the target was unchanged after the translation operation, the reconstructed RCS pattern in Fig. 8(b) is exactly same as those presented in Fig. 4(b).

E. Image Filtering and Insertion

Other important operations are image filtering and insertion, where the former refers to the extraction of a desired portion of an image by applying a spatial window to the image, and the latter means the replacement of a part of a image with another image. Note that the spatial filtering of a radar image was also investigated in [2], [16], [18].

For example, we consider the following circular "band-pass" filter function of radius ρ_Π centered at the spatial origin $(0, 0)$:

$$\Pi(x, y) = \begin{cases} 1, & \sqrt{x^2 + y^2} < \rho_\Pi \\ 0, & \text{otherwise.} \end{cases} \quad (23)$$

Similarly, the following circular "band-stop" filter function can be defined:

$$\Pi^c(x, y) = \begin{cases} 0, & \sqrt{x^2 + y^2} < \rho_\Pi \\ 1, & \text{otherwise.} \end{cases} \quad (24)$$

If our objective is to extract or reject a circular region of radius ρ_Π centered at (x_c, y_c) from the spatial image $\psi(x, y)$, the following operation can be used:

$$\psi_\Pi(x, y) = \Pi(x - x_c, y - y_c)\psi(x, y) \quad (25a)$$

$$\psi_{\Pi^c}(x, y) = \Pi^c(x - x_c, y - y_c)\psi(x, y) \quad (25b)$$

Note that other 2-D spatial filter functions, such as a rectangular, elliptical, and Gaussian window, are applicable as well.

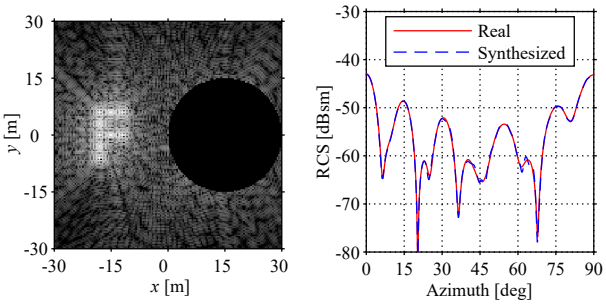

(a) (b)

Fig. 10. Band-stop filtered image and RCS (F-shaped scatterer created from FJ-shaped scatterer). (a) Spatial image. (b) RCS determined from (a).

Figs. 10 and 9 show the band-pass and band-stop filtered images of the FJ-shaped scatterer of Fig. 6(a) and the corresponding RCS, where the J- and F-portion were extracted, respectively, using the filter radius $\rho_\Pi = 15\,\text{cm}$ centered at $(x_c, y_c) = (15, 0)\,\text{cm}$. The reconstructed RCS in Figs. 10(b) and 9(b) exactly agree with the real RCS, and the patterns are same as those presented in Figs. 5(b) and 4(b), respectively, indicating the validity of the filtering approach.

Next, we explain the image insertion which is a combination of a spatially filtered image and another transformed image. As an example, we created an "FF"-shaped synthesized image by coherently adding the translated F-shaped image shown in Fig. 8(a) and the band-stop filtered image depicted in 10(a). The resultant image and RCS are represented in Figs. 11(a) and (b), respectively. By comparing the synthesized and real RCS shown in Fig. 11(b), we can confirm that the RCS of the FF-shaped scatterer is correctly recovered from the synthesized image, demonstrating the effectiveness of the proposed approach.

F. Frequency-Domain Synthesis

Before moving on to the experimental validation, we note the frequency-domain synthesis approach instead of the spatial-domain synthesis discussed so far. When we need to synthesize two images such that these are considerably separated away from each other, simply generating a large spatial image is an unsuitable option because such an image contains many redundant pixels with zero. In this case, image

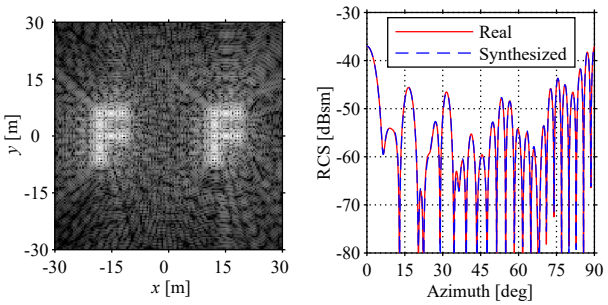

(a) (b)

Fig. 11. Inserted image and RCS (FF-shaped scatterer). The translated F-shaped base image of Fig. 8(a) was inserted to the band-stop filtered image of Fig. 10(a). (a) Spatial image. (b) RCS determined from (a).

synthesis can be efficiently done in the frequency domain without adding the large amount of zero-valued pixels.

By substituting the translated image defined in Eq. (22) into the NFFFT equation of Eq. (16), the RCS $\sigma_{\parallel}(k_x, k_y)$ of an translated image $\psi_{\parallel}(x, y)$ is expressed as follows:

$$\sigma_{\parallel}(k_x, k_y) = k^4 \left|\Psi_{\parallel}(k_x, k_y)\right|^2 \tag{26}$$

where

$$\Psi_{\parallel}(k_x, k_y) = e^{-jk_x x' - jk_y y'} \mathcal{F}^{-1}_{(x,y)} \left[\psi(x, y)\right] \tag{27}$$

is the translated image in the spatial frequency domain.

As an example, let us consider generating a synthesized image from a set of translated images $\psi_{\parallel,m}(x, y), m \in \{1, 2, \ldots\}$ of a base image $\psi(x, y)$, where the amount of translation for the mth image is (x'_m, y'_m). In this case, the corresponding mth frequency-domain image $\Psi_{\parallel,m}(k_x, k_y)$ is

$$\Psi_{\parallel,m}(k_x, k_y) = e^{-jk_x x'_m - jk_y y'_m} \mathcal{F}^{-1}_{(x,y)} \left[\psi(x, y)\right]. \tag{28}$$

Using the frequency-domain image $\Psi_{\parallel,m}(k_x, k_y)$ defined in Eq. (28), the synthesized RCS $\sigma_{\Sigma}(k_x, k_y)$ can be computed via the following expression:

$$\sigma_{\Sigma}(k_x, k_y) = k^4 \left|\sum_m \Psi_{\parallel,m}(k_x, k_y)\right|^2 \tag{29}$$

In this approach, padding a large amount of zeros in the base image to reserve a space for long-range translation is unnecessary.

Note that this frequency-domain RCS synthesis is similar to the array-factor-based algorithm discussed in [14], [15], where a numerically simulated complex-valued scattering pattern was used to synthesize the RCS of a cluster of multiple targets. The major merit of the image-based RCS synthesis presented in this article compared to the previous work is the availability of the spatial filtering which is a distinctive feature of generating the radar image, as presented in Section III-E.

In the following discussion, we only employed the spatial-domain synthesis for simplicity.

IV. Experimental Validation

In this section, we discuss experimental validation of the proposed algorithm.

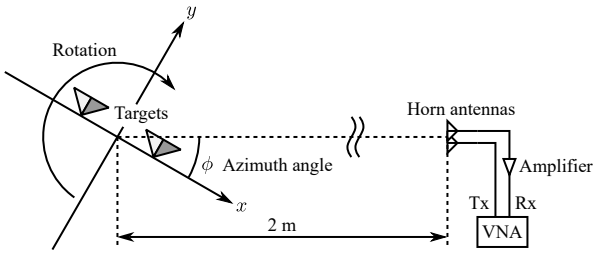

Fig. 12. Experimental setup.

TABLE II
Experimental Parameters

Polarization	HH
Center frequency	10.2 GHz
Bandwidth	4 GHz
Frequency sampling interval	20 MHz
Angular sampling interval	0.4°
Angular range	[0°, 360°]
Radius of trajectory	2 m

A. Overview of the Experiment

Fig. 12 illustrates the experimental setup, and Fig. 13 depicts the photographs of the experiment; the experimental parameters are listed in Table II. These parameters are exactly same as those employed in the numerical simulation presented in Section III. The experiments were carried out in an anechoic chamber.

As shown in Fig. 12, a single target or multiple targets were placed around the origin of the 2-D (x, y)-plane, and the transmitting and receiving antennas were fixed at 2 m away from the origin. As shown in Fig. 13(a), targets were deployed on a styrene foam support mounted on a turntable and rotated to create a circular synthetic aperture. The angular sampling interval was 0.4°.

As shown in Fig. 13(b), two standard gain horn antennas (Model 640, Narda-MITEQ, USA) were mounted on a tripod. The radiation pattern for these antennas was calculated using a theoretical expression given in [20], and the pattern was used as $P(k, \boldsymbol{r}_0, \boldsymbol{r})$ in the image reconstruction defined in Eq. (7). The antennas were aligned such that the backscattering for horizontally polarized transmission and reception (HH) can be measured. These antennas where connected to a vector network analyzer (VNA, N5225B, Keysight Technologies, USA) through microwave coaxial cables. As illustrated in Fig. 12, a 25 dB-gain power amplifier (GT-1040A, Giga-tronics, USA) was inserted in the receiving path. The center frequency was 10.2 GHz, and the bandwidth was 4 GHz, where the frequency sampling interval was 20 MHz.

The general strategy of this experiment was as follows: First, we measured a single target to create a base image. Then, according to the algorithm presented in Section III, we synthesized an image in which multiple targets were virtually deployed, followed by the computation of the corresponding RCS. Finally, the accuracy of the reconstructed RCS was evaluated by comparing it with the real RCS determined from a real image obtained by an experiment where multiple targets

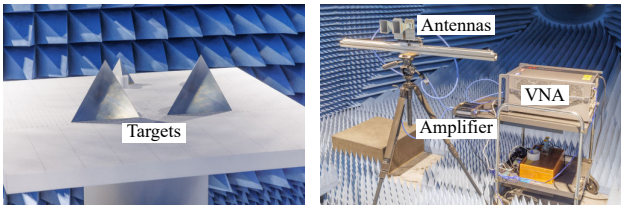

(a) (b)

Fig. 13. Photographs of the experiment. (a) Targets. (b) VNA, horn antennas, and amplifier.

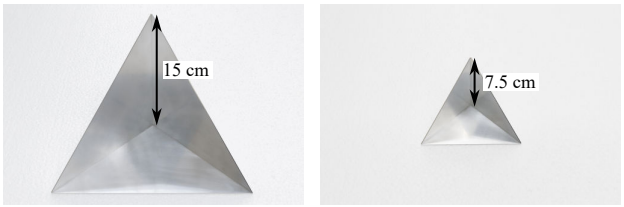

(a) (b)

Fig. 14. Photographs of the trihedrals. (a) Large trihedral. (b) Small trihedral.

were actually placed.

The following mean error σ_e was used for the evaluation:

$$\sigma_e = \frac{1}{N}\sum_{n=1}^{N} \left|\sigma_{\mathrm{dB}}[n] - \widetilde{\sigma}_{\mathrm{dB}}[n]\right|, \tag{30}$$

where $\sigma_{\mathrm{dB}}[n]$ and $\widetilde{\sigma}_{\mathrm{dB}}[n]$ represent the nth sample of the RCS pattern defined in dBsm-scale reconstructed from a real and a synthesized image, respectively; N is the total number of the samples. Note that throughout this experimental validation, the RCS was computed at $10\,\mathrm{GHz}$.

B. RCS Synthesis of Trihedrals

In this section, trihedral reflectors were employed for demonstration. Various arrangements were tested to show the validity and limitation of the proposed image-based RCS synthesis. Fig. 14 shows the photographs of the trihedrals. A $15\,\mathrm{cm}$- and $7.5\,\mathrm{cm}$-trihedral were used, where we refer to them as a large and a small trihedral, respectively.

1) Base Images and RCS: First, we show the base images. In the measurement, the trihedral was aligned such that the axis of symmetry was along with the x-axis, the aperture was directed toward the positive x-direction, and the inner corner was coincide with the center of the rotation. The reconstructed base images are shown in Fig. 15, where (a) and (b) correspond to the image of the large and the small trihedral, respectively. The image intensity was normalized by the maximum value of the image of the large trihedral. The responses from these trihedrals are clearly imaged around the origin of the coordinate.

The RCS computed from the spatial images of Figs. 15(a) and (b) are displayed in Figs. 16(a) and (b), respectively, plotted with simulated RCS using a numerical electromagnetic solver for reference. The measured RCS generally agrees with the simulated one, indicating the validity of the image-based NFFFT used in this study.

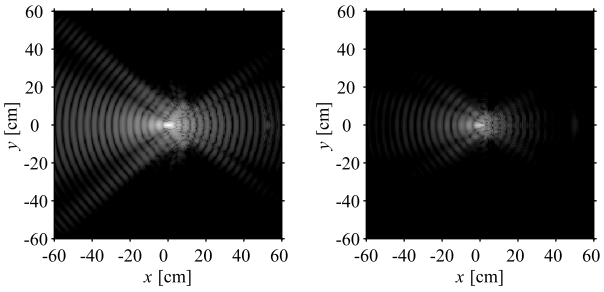

(a) (b)

Fig. 15. Base images (single large and small trihedral reflectors). The image was normalized by the maximum image intensity of the large trihedral. (a) Large trihedral. (b) Small trihedral.

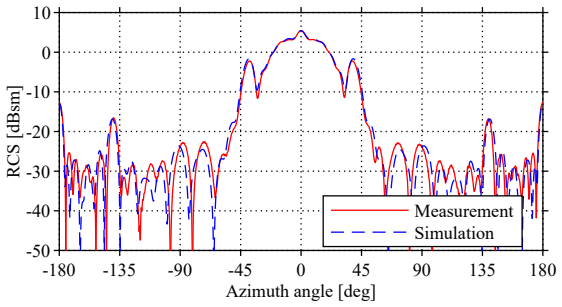

(a)

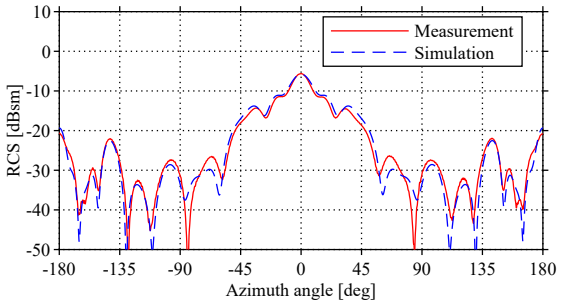

(b)

Fig. 16. RCS of the base images (trihedral reflectors). (a) Large trihedral. (b) Small trihedral.

2) Synthesis of Two Trihedrals: Next, we provide simple examples of the image-based RCS synthesis where the two large trihedrals were deployed. Using the base image shown in Fig. 15(a), we synthesized two different layouts shown in Fig. 17, where (a) illustrates two trihedrals on the x-axis of which the apertures were directed toward the positive y-direction (i.e., $90°$-direction), and (b) depicts the similar trihedrals but both of the apertures were directed toward the positive x-direction (i.e., $0°$-direction).

Figs. 18(a) and (b) show the real and the synthesized image corresponding to the cases shown in Figs. 17(a) and (b), respectively. As the trihedrals were sufficiently separated from each other, we can hardly notice the difference between these images. Therefore, similar RCS patterns were expected to be obtained.

Fig. 19 compares the real and the synthesized RCS re-

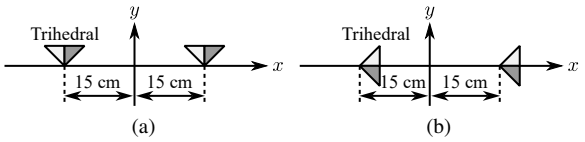

Fig. 17. Layout of the fixed two large trihedrals. (a) y-directed trihedrals. (b) x-directed trihedrals.

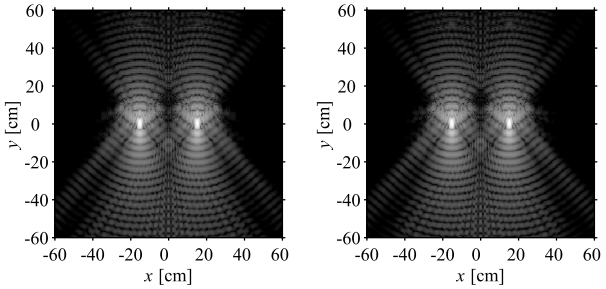

Fig. 18. Real and synthesized images (y-directed large trihedrals). (a) Real image. (b) Synthesized image.

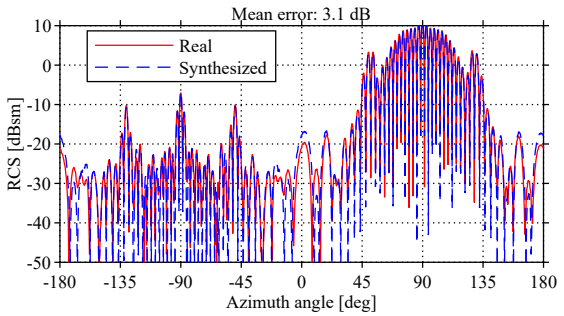

Fig. 19. Real and synthesized RCS (y-directed large trihedrals).

constructed from the images shown in Figs. 18(a) and (b), respectively. As the distance between the two trihedrals were considerably large ($30\,\mathrm{cm} \simeq 10\lambda$ at $10\,\mathrm{GHz}$) compared to the operating wavelength, the obtained RCS shows the rapidly oscillating nature for the entire azimuth angle. In this arrangement, the aperture of the one trihedral was never masked by that of the another reflector, though their apertures were pointed toward the same direction (i.e., $90°$-direction).

As the real and the synthesized RCS in Fig. 19 exhibit the almost same pattern, the validity of the proposed RCS synthesis is understood. However, a close examination around $0°$ and $\pm 180°$ reveals that the real RCS values at these angles are approximately 3-dB lower than the synthesized RCS. As was expected, this difference was attributed to the shadowing effect where the one trihedral was invisible from the antennas because the another trihedral was laid between them. The mean RCS error for this case was $3.1\,\mathrm{dB}$.

Similarly, Figs. 20(a) and (b) show the real and the synthesized image corresponding to the case shown in Fig. 17(b), respectively. Unlike Fig. 18, the trihedral on the left in Fig. 20(a) exhibits the weaker intensity compared to that in Fig.

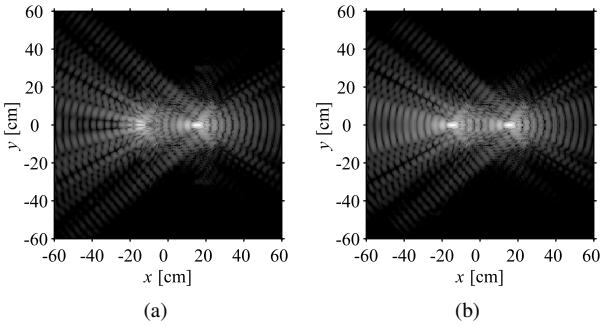

Fig. 20. Real and synthesized images (x-directed large trihedral reflectors). (a) Real image. (b) Synthesized image.

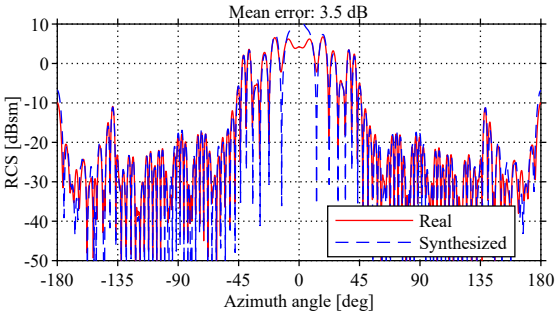

Fig. 21. Real and synthesized RCS (x-directed large trihedrals).

20(b). Since the both trihedrals were on the x-axis and the their apertures were pointed toward the positive x-direction (i.e., $0°$-direction), the main beam of the left trihedral was blocked by the right trihedral. Therefore, the different image intensity was obtained in this case. In contrast, since the synthesized image was unable to take this shadowing effect into account, the both trihedrals represent the identical image intensity, as displayed in Fig. 20(b).

The difference of the image intensity affected the reconstructed RCS. Fig. 21 compares the RCS reconstructed from the real and the synthesized image shown in Figs. 20(a) and (b), respectively. One can readily recognize the difference around the azimuth angle $0°$, where the real RCS is approximately 7-dB lower than the synthesized RCS at $0°$. As discussed before, this phenomenon is attributed to the fact that the main beam of the left trihedral was masked by the right trihedral. Although the RCS patterns differ around $0°$, the patterns at other azimuth angles well agree with each other. In this case, the mean RCS error was $3.5\,\mathrm{dB}$.

3) Effect of the Distance Between Trihedrals: Here, we consider a more difficult situation to investigate the limitation of the proposed algorithm in detail. As illustrated in Fig. 22, two large trihedrals were deployed, where the lower one was on the x-axis, and the upper one was on the y-axis at $y = 30\,\mathrm{cm}$ which was approximately 10λ at $10\,\mathrm{GHz}$. Their apertures were directed toward the opposite directions, that is, the upper and lower trihedrals pointed toward the negative and positive y-directions (i.e., $270°$- and $90°$-direction), respectively. As the main beams of these trihedrals were opposite

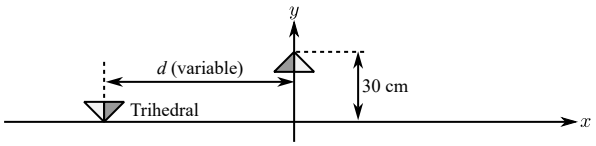

Fig. 22. Layout of the two large trihedrals directed toward the opposite directions. The horizontal distance d between them was variable.

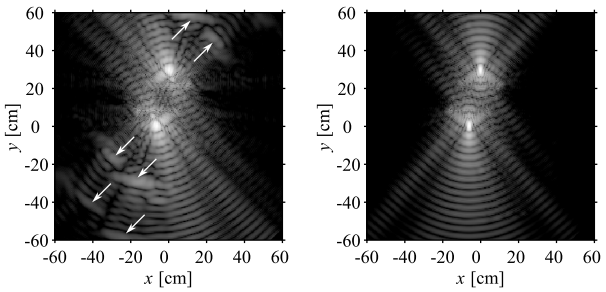

Fig. 23. Real and synthesized images (two large trihedrals with variable separation, $d = 6\,\mathrm{cm}$). Arrows in (a) designate the locations where multiple scattering responses are apparent. (a) Real image. (b) Synthesized image.

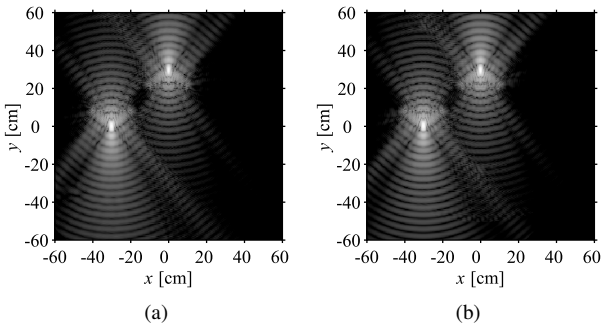

Fig. 24. Real and synthesized images (two large trihedrals with variable separation, $d = 30\,\mathrm{cm}$). (a) Real image. (b) Synthesized image.

to each other, severe shadowing effect were expected to be occurred when the distance was too short. Based on this layout, the lower trihedral was moved along the x-axis to change the horizontal distance d between the two targets.

Figs. 23 and 24 compare the (a) real and (b) the synthesized image when the horizontal separation between the trihedrals were $d = 6\,\mathrm{cm} \approx 2\lambda$ and $d = 30\,\mathrm{cm} \approx 10\lambda$, respectively. As shown in Fig. 23, the real and the synthesized image for this case are considerably different from each other. By comparing the peaks at the corner of the trihedrals in Figs. 23(a) and (b), one can recognize that the responses of the real image in Fig. 23(a) are broader than that of the synthesized image in Fig. 23(b). This broadening was because that the main lobe of the one reflector was masked by that of the another reflector, shortening the effective synthetic aperture length to extend the point spread function.

Another characteristic feature of the real image in Fig. 23(a) compared to the synthesized image in Fig. 23(b) is that the multiple scattering between the reflectors is presented in the

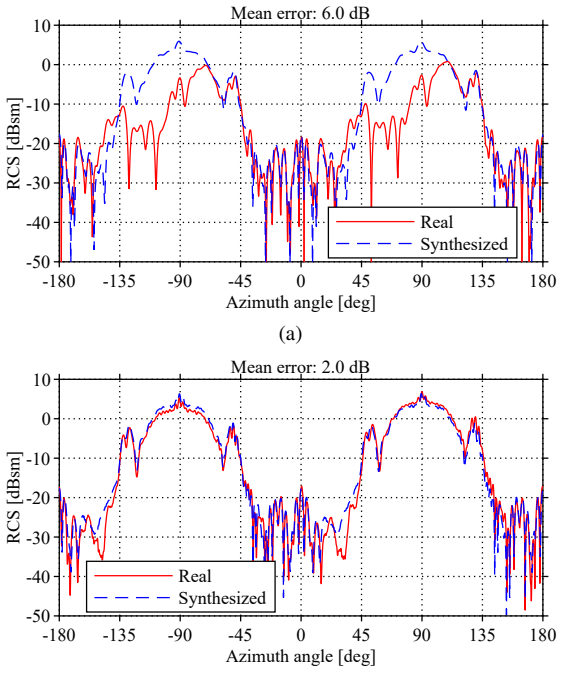

Fig. 25. Real and synthesized RCS (two large trihedrals with variable separation). (a) $d = 2\lambda$. (b) $d = 10\lambda$.

real image, as indicated by the arrows in Fig. 23(a). As these shadowing and multiple scattering effect were unable to be incorporated into the synthesized image, the RCS patterns obtained from the real and the synthesized image were expected to be significantly different as well. In contrast to Fig. 23, the real and the synthesized image shown in Fig. 24 are almost identical. In this case, we can expect that the real and the synthesized RCS agree with each other.

Figs. 25(a) and (b) represent the RCS reconstructed from the spatial images shown in Figs. 23 and 24, respectively. As expected from the previous discussion, the real and the synthesized RCS are considerably different from each other in Fig. 25(a) which is the case when the horizontal separation $d = 2\lambda$. Owing to the shadowing effect, a portion of the main lobe of one trihedral reflector in the direction from that reflector toward the another one was seriously attenuated compared to the synthesized RCS. In this case, the mean RCS error was $6.0\,\mathrm{dB}$. On the other hand, the real and the synthesized RCS are almost same in Fig. 25(b), as expected; the mean RCS error in this case was $2.0\,\mathrm{dB}$.

Fig. 26 shows the mean error between the real and the synthesized RCS as a function of the horizontal distance d between the trihedral reflectors. Note that the distance d was normalized by the wavelength $\lambda \approx 3\,\mathrm{cm}$ at $10\,\mathrm{GHz}$. The mean error is reduced as the increase in the horizontal separation d. If a mean error $2\,\mathrm{dB}$ or lower was required, the reflectors must be separated 10λ or longer away from each other.

4) Target Rejection and Insertion: In this example, we demonstrate the concept of the target rejection and insertion using the spatial filtering established in Section III-E. Fig. 27 illustrates the experimental layout, where Fig. 27(a) shows

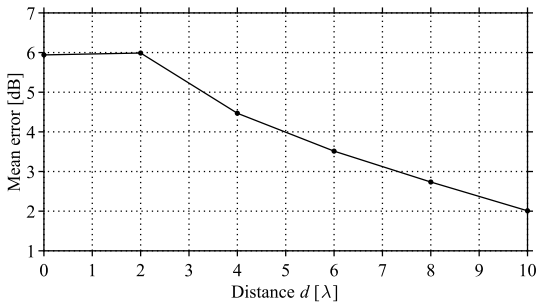

Fig. 26. Mean RCS error (two large trihedrals with variable separation). The wavelength λ at 10 GHz was assumed to normalize the distance d.

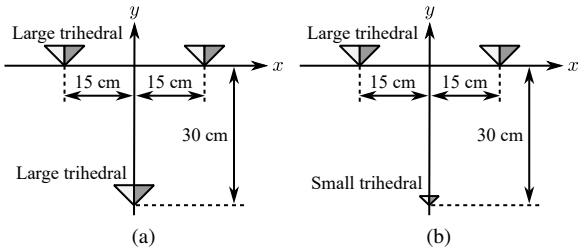

Fig. 27. Layout of the three trihedrals. (a) Three large trihedrals. (b) Two large trihedrals and one small trihedral.

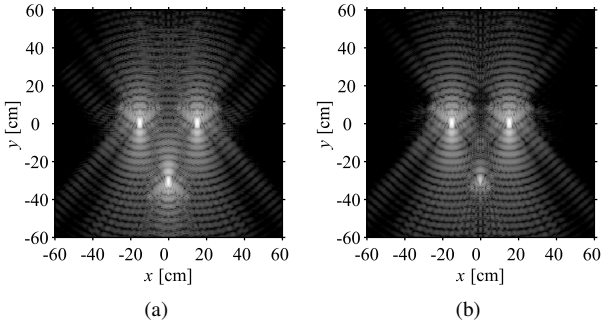

Fig. 28. Synthesized images (three trihedrals). Similar real images were obtained for these cases. (a) Three large trihedrals. (b) Two large trihedrals and one small trihedral.

three large trihedrals, and Fig. 27(b) shows two large trihedrals on the x-axis and one small trihedral on the negative y-axis. The synthesized images corresponding to Figs. 27(a) and (b) are presented in Figs. 28(a) and (b), respectively. Note that we have omitted to provide the real images as we confirmed that the real and the synthesized image were almost identical. The RCS reconstructed from the image of Fig. 28(a) is displayed in Fig. 29 for the sake of the following discussion; the synthesized RCS in Fig. 29 well agrees with the real pattern, and the mean error was 2.2 dB.

Fig. 30(a) shows a filtered image of Fig. 28(b), where the response of the small trihedral on the y-axis was erased by applying a circular band-stop filter $\Pi^c(x, y)$ defined in Eq. (25b) with the radius $\rho_\Pi = 5\,\mathrm{cm}$ centered at $(x_c, y_c) = (0, -30)\,\mathrm{cm}$. The corresponding RCS is presented in Fig. 31(a), where the similar RCS patterns as those displayed in Fig. 19 were

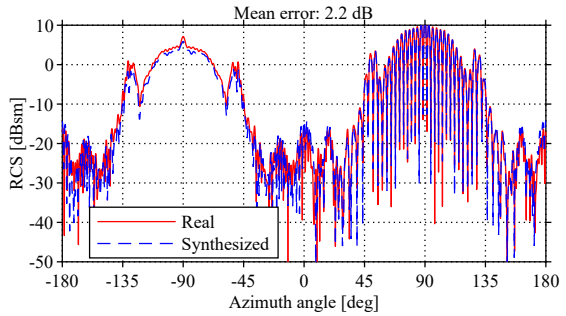

Fig. 29. Real and synthesized RCS (three trihedrals).

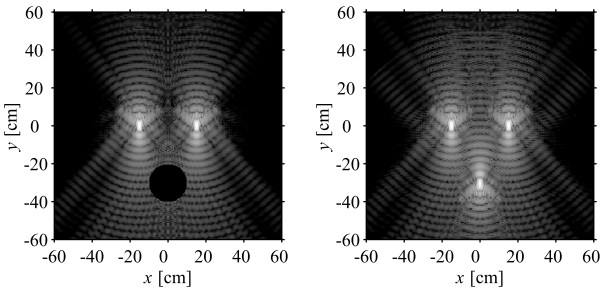

Fig. 30. Band-stop filtered and inserted images (three trihedrals). (a) Band-stop filtered image of Fig. 28(b). (b) Inserted image of (a).

obtained, showing the validity of the spatial filtering; the mean error was 1.5 dB for this case.

In Fig. 30(b), the base image of the large trihedral shown in Fig. 15(a) was inserted to emulate the image represented in Fig. 28(a) of which the layout is drawn in Fig. 27(a). The RCS reconstructed from the synthesized image of Fig. 30(b) is displayed in Fig. 31(b). As the reconstructed RCS patterns in Figs. 29 and 31(b) are almost identical, the validity of the proposed image-based RCS synthesis with the spatial filtering is proved; the mean error was 1.8 dB for this case.

In conclusion of the series of the experiments using trihedral reflectors discussed so far, the proposed image-based RCS synthesis functions properly when the mutual interactions between the targets can effectively be ignored, that is, the multiple reflection is not significant as the targets are sufficiently separated, and the major backscattering of a target is free from the shadowing by another object.

C. RCS Synthesis of Aircraft Models

As the final experiment, we show the synthesis of more complex targets—aircraft models.

1) Base Images and RCS: As depicted in Fig. 32, two aircraft models were used, where Fig. 32(a) and (b) show an aluminum- and resin-made model, respectively. The surface of the resin-made model were completely coated with highly conductive paint which contains silver-copper particles. This resin-made model was employed just for reducing the manufacturing cost. The length, height, and width of the model

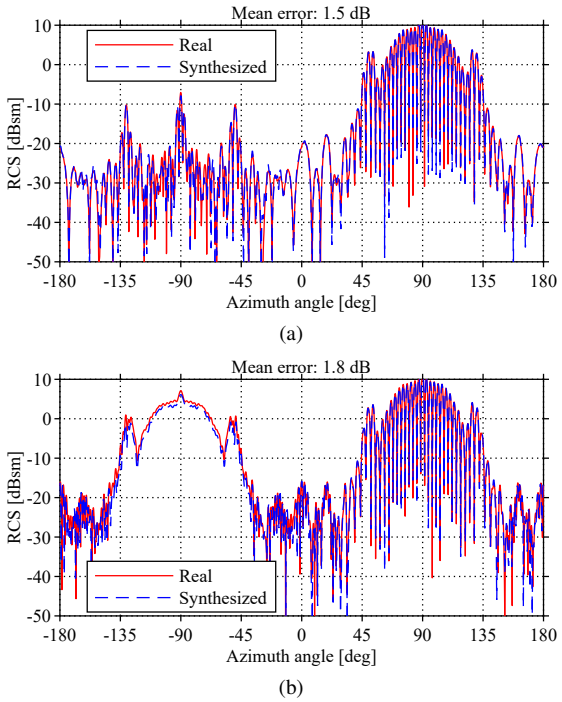

Fig. 31. Real and synthesized RCS (target rejection and insertion). (a) Obtained from Fig. 30(a). (b) Obtained from Fig. 30(b).

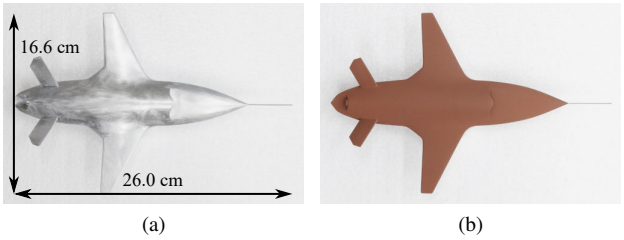

Fig. 32. Photographs of the aircraft models. (a) Aluminum-made model. (b) Resin-made model coated with conductive paint.

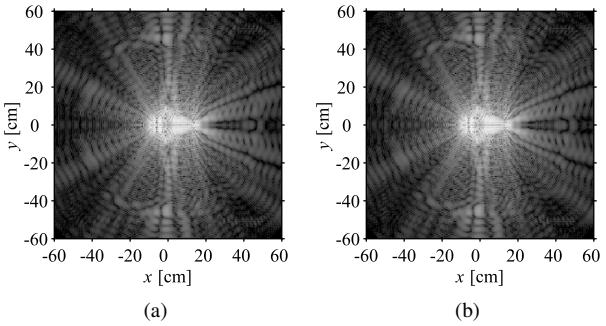

Fig. 33. Base images (aircraft models). (a) Aluminum-made model. (b) Resin-made model.

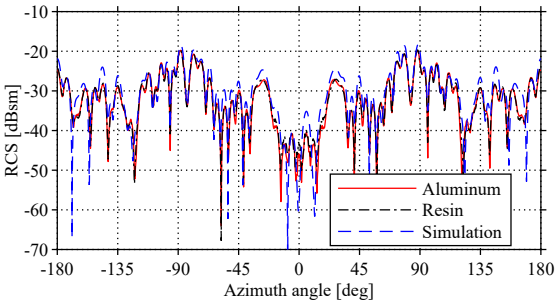

Fig. 34. RCS of the base images (aircraft models).

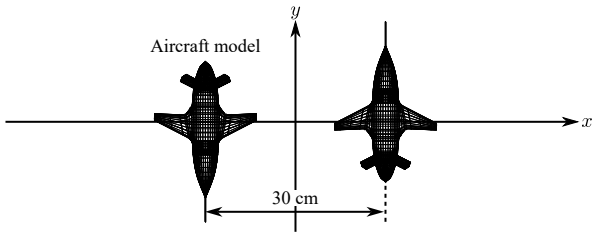

Fig. 35. Layout of the two aircraft models.

were 26.0 cm, 4.4 cm, and 16.6 cm, respectively, where the size was $1/40$ of the full-scale model. Note that the shape is similar to the model which was investigated in the literature [10]–[12].

Figs. 33(a) and (b) show the reconstructed base images for the aluminum- and resin-made aircraft model, respectively. Comparing Figs. 33(a) and (b) reveals that the almost identical images are obtained, representing the equivalence of these models. The corresponding RCS patterns are displayed in Fig. 33, plotted with the simulated RCS using a numerical electromagnetic solver. We can confirm that the measured RCS patterns are almost same, and these patterns well agree with the simulation.

2) Synthesis of Two Aircraft Models: As shown in Fig. 35, the two aircraft models were deployed on the x-axis, where the headings of the left- and right-side model were the negative and positive y-directions (i.e., 270°- and 90°-direction), respectively. The distance between the centers of these models were 30 cm which was approximately 10λ at 10 GHz.

Fig. 36 compares the real and the synthesized image of the two aircraft models. One can confirm that the almost identical images are obtained. Therefore, the resultant real and the synthesized RCS shown in Fig. 37 well agree with each other. The difference between the patterns is relatively large at 0° and ±180°, where around these azimuth angles, one aircraft model was shaded by the another model to reduce the accuracy of the RCS synthesis. The mean RCS error was 2.6 dB for this case of the two aircraft model. Therefore, the proposed RCS synthesis has shown to be also effective for an object with complex shape.

V. Conclusion

In this article, we proposed an image-based RCS synthesis algorithm for the prediction of backscattering from a cluster of multiple static targets. We first reconstructed an original radar image of a real target, and the image was repeatedly replicated and transformed to create multiple radar images; then, the copied and modified images were coherently summed to synthesize a single image which virtually contains all the scattering contributions from the transformed images, and the

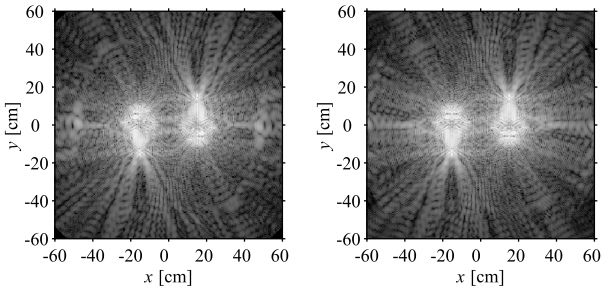

Fig. 36. Real and synthesized images (aircraft models). (a) Real image. (b) Synthesized image.

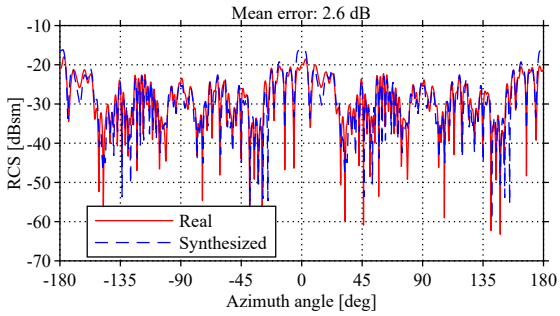

Fig. 37. Real and synthesized RCS (aircraft models).

2-D spatial Fourier transform of this synthesized image gave the RCS of the multiple targets. The numerical simulations and experimental validation showed the effectiveness of the proposed approach, provided that the mutual interactions between the targets such as the shadowing and multiple scattering effect were insignificant.

A 3-D generalization of the algorithm is straightforward but it requires a computationally intensive reconstruction of a 3-D image with a complete spherical antenna-scanning surface which is practically difficult to perform. An extension of the proposed approach to handle the shadowing effect is a possible future research. Moreover, polarimetric information can be utilized in the RCS synthesis.

REFERENCES

[1] D. G. Falconer, "Extrapolation of near-field RCS measurements to the far zone," *IEEE Trans. Antennas Propag.*, vol. 36, no. 6, pp. 822–829, Jun. 1988.

[2] H. Yamazaki and K. Koshiji, "Radar cross-section measurement method using a spatial filtering within a near zone," *IEEJ Trans. Electr. Electron. Eng.*, vol. 4, no. 1, pp. 107–113, 2009.

[3] G. Schnattinger, R. A. M. Mauermayer, and T. F. Eibert, "Monostatic radar cross section near-field far-field transformations by multilevel plane-wave decomposition," *IEEE Trans. Antennas Propag.*, vol. 62, no. 8, pp. 4259–4268, Aug. 2014.

[4] O. Neitz, R. A. M. Mauermayer, and T. F. Eibert, "3-D monostatic RCS determination from multistatic near-field measurements by plane-wave field synthesis," *IEEE Trans. Antennas Propag.*, vol. 67, no. 5, pp. 3387–3396, May 2019.

[5] S. Omi, M. Hirose, M. Ameya, and S. Kurokawa, "Plane-wave synthesis employing propagating plane-wave expansion for 3-D and 2-D RCS prediction including the multiple scattering effects," *IEEE Trans. Antennas Propag.*, vol. 69, no. 8, pp. 4827–4835, Aug. 2021.

[6] J. W. Odendaal and J. Joubert, "Radar cross section measurements using near-field radar imaging," *IEEE Trans. Instrum. Meas.*, vol. 45, no. 6, pp. 948–954, Dec. 1996.

[7] A. Broquetas, J. Palau, L. Jofre, and A. Cardama, "Spherical wave near-field imaging and radar cross-section measurement," *IEEE Trans. Antennas Propag.*, vol. 46, no. 5, pp. 730–735, May 1998.

[8] T. Vaupel and T .F. Eibert, "Comparison and application of near-field ISAR imaging techniques for far-field radar cross section determination," *IEEE Trans. Antennas Propag.*, vol. 54, no. 1, pp. 144–151, Jan. 2006.

[9] A. V. Osipov, H. Kobayashi, and H. Suzuki, "An improved image-based circular near-field-to-far-field transformation," *IEEE Trans. Antennas Propag.*, vol. 61, no. 2, pp. 989–993, Feb. 2013.

[10] T. Watanabe and H. Yamada, "Far-field radar cross-section determination from near-field 3-D synthetic aperture imaging with arbitrary antenna scanning surfaces," *IEEE Trans. Antennas Propag.*, vol. 70, no. 7, pp. 5831–5840, July 2022.

[11] T. Watanabe and H. Yamada, "Unified approach for multiscale radar cross-section measurement by synthetic aperture imaging," 2021, [Online]. Available: 10.36227/techrxiv.21127765.

[12] T. Watanabe and Y. Akamine, "Low-cost radar cross-section measurement with a resin-made model coated with conductive paste," 2022, [Online]. Available: 10.36227/techrxiv.21127765.

[13] I. J. LaHaie, "Overview of an image-based technique for predicting far-field radar cross section from near-field measurements," *IEEE Antennas Propag. Mag.*, vol. 45, no. 6, pp. 159–169, Dec. 2003.

[14] H. Suenobu, T. Tanaka, M. Takikawa, and N. Yoneda, "Radar cross section analysis of small group target," *in Proc. 2019 URSI Int. Symp. Electromagn. Theory (EMTS)*, May 2019, pp. 1–4.

[15] H. Suenobu, T. Tanaka, S. Yamamoto, M. Takikawa, and Y. Inasawa, "A study on radar cross section analysis of group target using array synthesis," *IEICE Trans. Commun.*, vol. J104-B, no. 11, pp. 889–896 (in Japanese), Nov. 2021.

[16] M. Soumekh, *Synthetic Aperture Radar Signal Processing: with MATLAB Algorithms*, Hoboken, NJ, USA: Wiley, 1999.

[17] M. Cheney and B. Borden, *Fundamentals of Radar Imaging*, Philadelphia, PA, USA: SIAM, 2009.

[18] T. Watanabe, H. Yamada, Y. Tokutake, R. Sato, and Y. Yamaguchi, "Retrieval of polarimetric azimuthal angular characteristics via the application of target decomposition to spectral domain circular SAR images," *IEEE Trans. Geosci. Remote Sens.*, vol. 57, no. 5, pp. 2963–2982, May 2019.

[19] G. T. Ruck, D. E. Barrick, W. D. Stuart, and C. K. Krichbaum, *Radar Cross Section Handbook*, vol. 1, New York, NY, USA: Plenum Press, 1970.

[20] C. A. Balanis, *Antenna Theory: Analysis and Design*, 4th ed., Hoboken, NJ, USA: Wiley, 2016.

[21] A. Tanaka, M. Kameyama, S. Kazama, and O. Watanabe, "A rotation method for raster image using skew transformation," *in Proc. IEEE Conf. Comp. Vision Patt. Recog.*, 1986, pp. 272–277.

[22] A. W. Peath, "A fast algorithm for general raster rotation," *in Proc. Graphics Interface '86*, pp. 77–81, Vancouver, 1986.

[23] K. G. Larkin et al., "Fast Fourier method for the accurate rotation of sampled images," *Opt. Commun.*, vol. 139, no. 1, pp. 99–106, Jun. 1997.

[24] T. Toffoli and J. Quick, "Three-dimensional rotations by three shears," *Graphical Models and Image Processing*, vol. 59, no. 2, pp. 89–95, Mar. 1997.

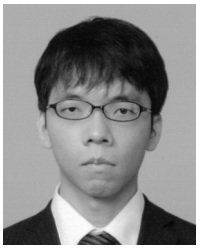

Takuma Watanabe (Member, IEEE) received the B.E., M.E., and Ph.D. degrees in electrical and information engineering from Niigata University, Niigata, Japan, in 2010, 2012, and 2015, respectively.

From 2015 to 2017, he worked with the Central Research Institute of Electric Power Industry, Yokosuka, Japan. From 2017 to 2018, he worked with PASCO Corporation, Tokyo, Japan. Since 2018, he has been with Fujitsu Ltd., Kawasaki, Japan, and since 2021, he has been with Fujitsu System Integration Laboratories Ltd., Kawasaki, where he is currently a Research Scientist. His research interests include image reconstruction problems, synthetic aperture radar (SAR) signal processing, array signal processing, and electromagnetic scattering problems.